

pubs.acs.org/JACS Article

Improvement of Oxygen Reduction Performance in Alkaline Media by Tuning Phase Structure of Pd-Bi Nanocatalysts

Ming Zhou, [⊥] Jiangna Guo, [⊥] Bo Zhao, Can Li, Lihua Zhang,* and Jiye Fang*



Cite This: J. Am. Chem. Soc. 2021, 143, 15891–15897



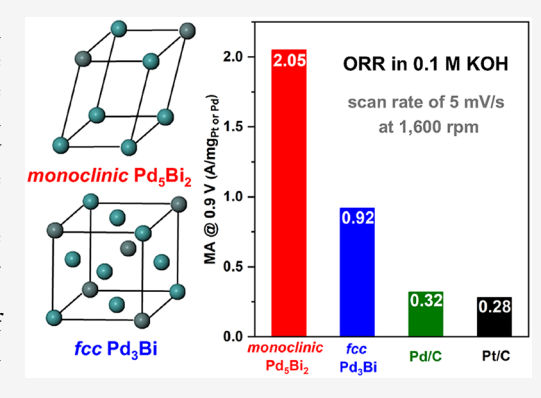
ACCESS

Metrics & More

Article Recommendations

Supporting Information

ABSTRACT: Tuning the crystal phase of bimetallic nanocrystals offers an alternative avenue to improving their electrocatalytic performance. Herein, we present a facile and one-pot synthesis approach that is used to enhance the catalytic activity and stability toward oxygen reduction reaction (ORR) in alkaline media via control of the crystal structure of Pd–Bi nanocrystals. By merely altering the types of Pd precursors under the same conditions, the monoclinic structured Pd₅Bi₂ and conventional face-centered cubic (fcc) structured Pd₃Bi nanocrystals with comparable size and morphology can be precisely synthesized, respectively. Interestingly, the carbon-supported monoclinic Pd₅Bi₂ nanocrystals exhibit superior ORR activity in alkaline media, delivering a mass activity (MA) as high as 2.05 A/mg_{Pd}. After 10,000 cycles of ORR durability test, the monoclinic structured Pd₅Bi₂/C nanocatalysts still remain a MA of 1.52 A/mg_{Pd}, which is 3.6 times, 16.9 times, and 21.7 times as high as those of the fcc Pd₃Bi/C counterpart, commercial Pd/C, and Pt/C



electrocatalysts, respectively. Moreover, structural characterizations of the *monoclinic* Pd_5Bi_2/C nanocrystals after the durability test demonstrate the excellent retention of the original size, morphology, composition, and crystal phase, greatly alleviating the leaching of the Bi component. This work provides new insight for the synthesis of multimetallic catalysts with a metastable phase and demonstrates phase-dependent catalytic performance.

1. INTRODUCTION

Pt-based nanocrystals have been recognized as efficient and promising catalysts used in proton-exchange membrane fuel cells (PEMFCs) due to their high catalytic activity toward oxygen reduction reaction (ORR) at the cathodes. 1-5 To accelerate the sluggish ORR kinetics, a significant amount of scarce Pt (>0.2 g/kW) in the catalysts is typically required, 6-9 and it is critical for the broad-based applications of PEMFCs by persistently searching for Pt-reduced or Pt-free ORR electrocatalysts. Alternatively, Pd-based nanocrystals have emerged as particularly promising electrocatalysts for the ORR especially in alkaline media. $^{10-13}$ To further improve the ORR performance of Pd-based electrocatalysts, tremendous efforts have been continuously dedicated to engineering the catalyst component and structure (such as incorporating another less expensive metal to form an alloyed or coreshell structure) and controlling size and morphology. 14-18 As such, a variety of bimetallic or multimetallic Pd-based nanocrystals with controlled structural parameters have been deliberately synthesized and shown substantially enhanced activities toward ORR in alkaline media. For example, Guo and co-workers synthesized the superthin PdMo nanosheets with the subnanometric thickness using a wet-chemical approach, greatly boosting both the mass activity (MA) and durability as compared to the commercial Pd/C and Pt/C catalysts.¹¹ Abruña et al. prepared Pd/M (M = Ni, Mn) core-shell nanoparticles utilizing an electrochemical dealloying approach and demonstrated high electrocatalytic activity. On the other hand, most Pd-based electrocatalysts possess a thermodynamically stable *fcc* phase, and they face a challenge of transition metal leaching during the reaction process, which could cause severe deactivation of catalysts. Relative to the conventional *fcc* phase, it was reported that the thermodynamically unstable phases might present entirely different electronic structures, dramatically improving their catalytic activities and chemical/structural stabilities. This could also effectively mitigate the leaching problem. Therefore, an elaborate design of Pd-based electrocatalysts with a desirable structure could be an alternative strategy to further develop the ORR electrocatalysts.

The synthesis of Pd-based nanocrystals with a metastable structure is highly challenging due to the competitive formation of the thermodynamically stable phase. In recent years, considerable efforts have been made on the development

Received: August 16, 2021 Published: September 14, 2021





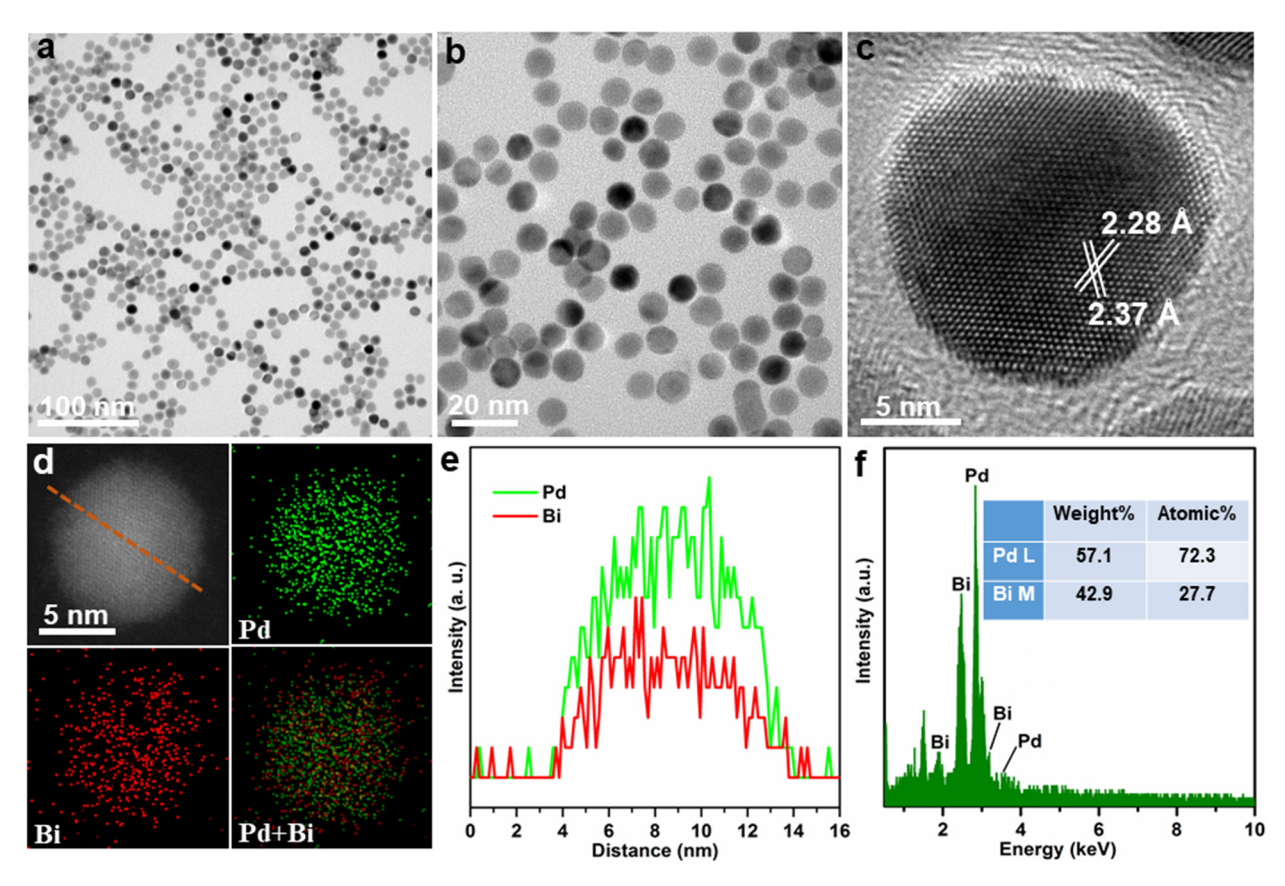


Figure 1. (a) Low-magnification and (b) high-magnification TEM images of the *monoclinic* Pd_5Bi_2 nanocrystals. (c) HRTEM image of a representative *monoclinic* Pd_5Bi_2 nanocrystal. (d) STEM image and the corresponding elemental mappings of a typical *monoclinic* Pd_5Bi_2 nanocrystal. (e) EDX line scan across an individual *monoclinic* Pd_5Bi_2 nanocrystal as indicated by the dashed line in (d). (f) The corresponding STEM-EDS spectrum of the *monoclinic* Pd_5Bi_2 nanocrystals. The inset in (f) shows the weight and atomic percentages of the Pd and Bi elements in *monoclinic* Pd_5Bi_2 nanocrystals.

of effective methods in the crystal phase control, such as hightemperature annealing, high pressure-induced phase transformation, and electrodeposition. ^{23,27–29} The resultant products from these methods often show irregular shapes and larger particle sizes with a broad range of size distribution, seriously impeding their catalytic performance. Unlike these approaches, one-pot synthesis possesses advantages in its versatility, precise control over size, shape, composition, surface and crystal structures in the final products, and easy scaling-up.³ However, this synthesis protocol has been rarely applied to the preparation of metastable Pd-based nanocrystals that could be particularly beneficial for the ORR performance. In this report, we present our synthesis of both monoclinic structured Pd₅Bi₂ and fcc structured Pd3Bi nanocrystals using this one-pot approach, and demonstrate the advantage of the resultant monoclinic Pd₅Bi₂/C toward ORR.

2. RESULTS AND DISCUSSION

In a typical one-pot synthesis of the metastable *monoclinic* Pd_5Bi_2 nanocrystals (*vide infra*), K_2PdCl_4 , $Bi(NO_3)_3 \cdot SH_2O$, NH_4Br , and poly(vinylpyrrolidone) were codissolved in ethylene glycol (EG). The as-obtained mixture was then heated in an oil bath at 160 °C for 3 h. The color of the solution turned dark brown immediately upon heating, implying quick formation of metallic nanocrystals due to the fast reduction by EG at the high temperature. Figures 1a and 1b show the transmission electron microscopy (TEM) images of the metastable *monoclinic* Pd–Bi nanocrystals in an average

diameter of 10.2 ± 1.3 nm with a narrow size and shape distribution (Figure S1). The high-resolution TEM (HRTEM) image taken from an individual nanocrystal along [001] zone axis is shown in Figure 1c, where the lattice spacings are measured to be 2.37 and 2.28 Å, corresponding to the (112) and (202) planes of the monoclinic Pd-Bi, respectively. These values also match well with the (112) and (202) lattice spacings calculated from the powder X-ray diffraction (XRD) pattern of the monoclinic Pd₅Bi₂, confirming the metastable monoclinic phase. Meanwhile, the HRTEM image clearly shows the continuous lattice extending across an individual nanocrystal in the same orientation, further revealing the singlecrystal structure with high crystallinity. Furthermore, we also validate the formation of an alloyed structure with the uniform distributions of Pd and Bi elements by analyzing an individual nanocrystal using energy-dispersive X-ray spectroscopy (EDX) mapping (Figure 1d) and line scan techniques (Figure 1e). Specifically, the Pd/Bi atomic ratio of Pd-Bi nanocrystals was determined to be 72.3:27.7 by scanning transmission electron microscopy-EDX (STEM-EDX) (Figure 1f), almost identical to the inductively coupled plasma-optical emission spectroscopy (ICP-OES) result (Pd/Bi atomic ratio = 72.1:27.9). Based on this result, the monoclinic nanocrystals are denoted as Pd₅Bi₂. It also reveals that the conversion of both the Pd(II) and Bi(III) precursors could reach a level of >99% with EG as the reductant in the one-pot synthesis.

Interestingly, by merely replacing the K₂PdCl₄ precursor with an equal mole of Pd(acac)₂ while other synthetic

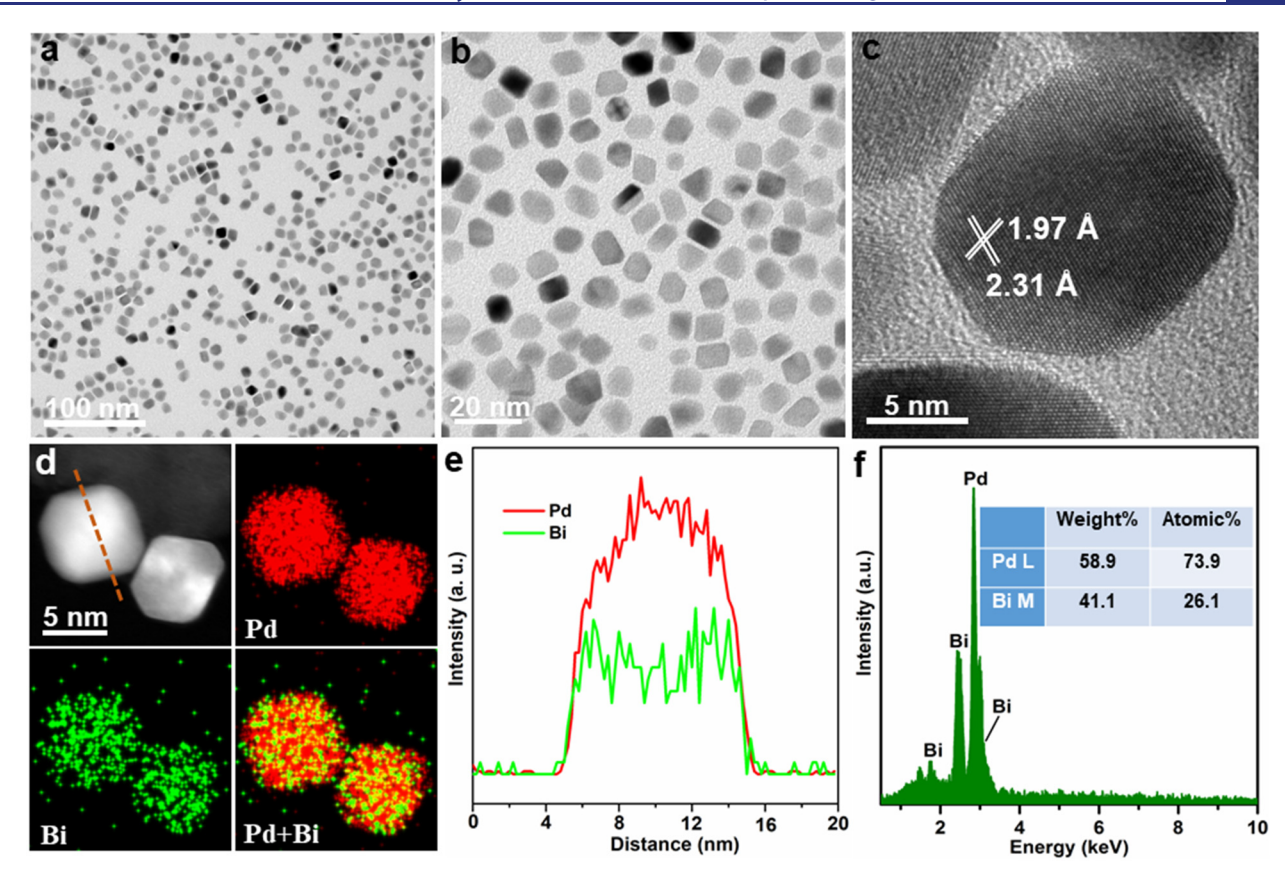


Figure 2. (a) Low-magnification and (b) high-magnification TEM images of the *fcc* Pd₃Bi nanocrystals. (c) HRTEM image of a representative *fcc* Pd₃Bi nanocrystal. (d) STEM image and the corresponding elemental mappings of two representative *fcc* Pd₃Bi nanocrystals. (e) EDX line scan across the *fcc* Pd₃Bi nanocrystals as indicated by the dashed line in (d). (f) The corresponding STEM-EDS spectrum of the *fcc* Pd₃Bi nanocrystals. The inset in (f) shows the weight and atomic percentages of the Pd and Bi elements in *fcc* Pd₃Bi nanocrystals.

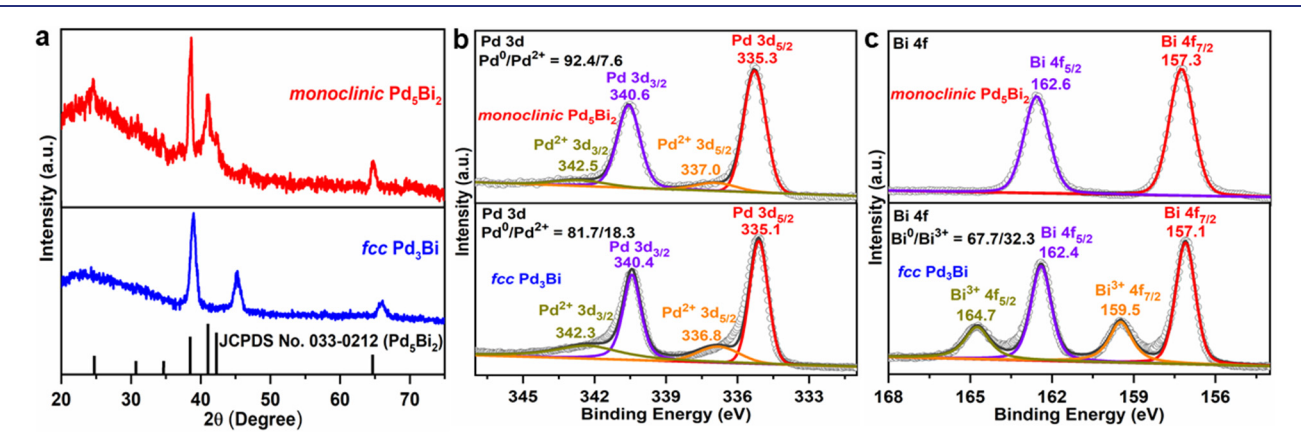


Figure 3. (a) XRD patterns of the *monoclinic* Pd₅Bi₂ and *fcc* Pd₃Bi nanocrystals. The lines on the bottom show standard XRD pattern of Pd₅Bi₂; (b, c) XPS spectra of Pd 3d (b) and Bi 4f (c) for the *monoclinic* Pd₅Bi₂ and *fcc* Pd₃Bi nanocrystals, respectively.

conditions were kept the same, conventional fcc Pd-Bi nanocrystals can be readily obtained with comparable size, morphology, and composition. The TEM images (Figures 2a and 2b) suggest an average size of 11.1 ± 1.9 nm (Figure S2), with uniform size and shape distribution. As shown in the HRTEM image (Figure 2c), the clear lattice fringes with spacings of 2.31 and 1.97 Å nm can be indexed to the (111) and (200) planes of the fcc Pd₃Bi, respectively. S5,36 In this case, a single-crystal structure and high crystallinity across the entire fcc Pd-Bi nanocrystal can also be verified using the clear lattice fringes. Moreover, the EDX mapping (Figure 2d) and

corresponding EDX line scan (Figure 2e) reveal that the Pd and Bi elements are well distributed throughout the nanocrystal. The STEM-EDX result on the as-obtained fcc Pd-Bi nanocrystals suggests a Pd/Bi atomic ratio of 73.9:26.1 (Figure 2f), which is consistent with the measurement received from the ICP-OES analysis (Pd/Bi atomic ratio = 74.2:25.8). Therefore, the fcc nanocrystals can be approximately designed as Pd₃Bi. This composition result also indicates the conversions of Pd and Bi precursors dropped to 92% in the presence of Pd(acac)₂, demonstrating a slower reduction rate of Pd(acac)₂ compared to that of K_2 PdCl₄ in the EG system.

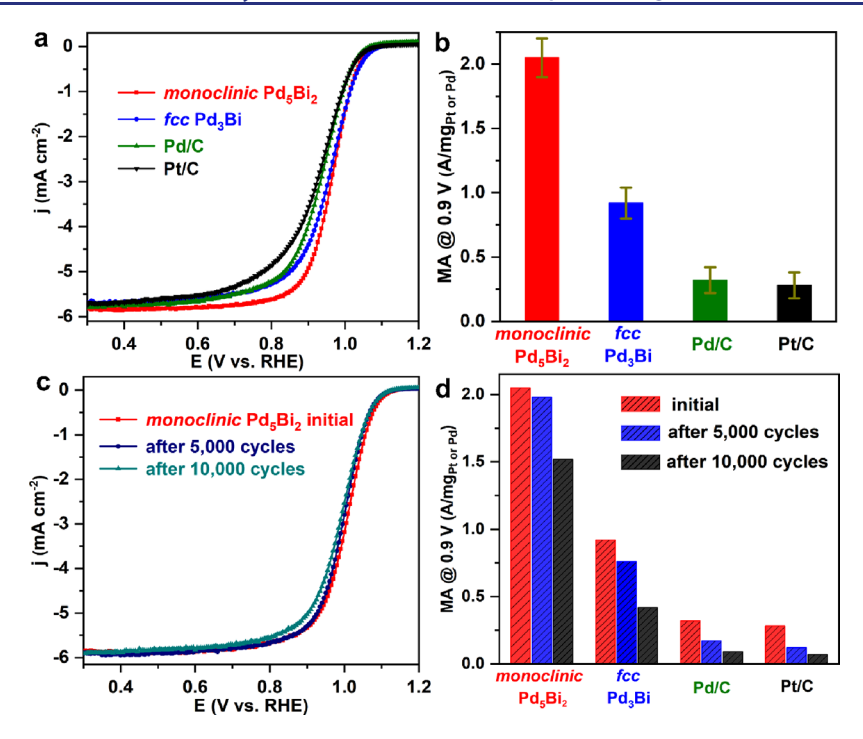


Figure 4. (a) ORR polarization curves of the *monoclinic* Pd_5Bi_2/C , fcc Pd_3Bi/C , Pd/C, and Pt/C, in O_2 -saturated 0.1 M KOH at a scan rate of 5 mV/s at 1,600 rpm. (b) Mass activities of the *monoclinic* Pd_5Bi_2/C , fcc Pd_3Bi/C , Pd/C, and Pt/C at 0.9 V vs RHE, which were calculated by normalizing the kinetic current to the mass loading on the electrode, respectively. (c) ORR polarization curves of the *monoclinic* Pd_5Bi_2/C before and after the accelerated durability tests in O_2 -saturated 0.1 M KOH at a scan rate of 100 mV/s from 0.6 to 1.0 V vs RHE. (d) Mass activities of the *monoclinic* Pd_5Bi_2/C , fcc Pd_3Bi/C , Pd/C, and Pt/C before and after the accelerated durability tests in O_2 -saturated 0.1 M KOH at 0.9 V vs RHE.

According to this investigation, the types of Pd precursors involved in the synthesis may play a significant role in steering the crystal phase formation in the resultant nanocrystals.

The crystal phases of the monoclinic Pd₅Bi₂ and fcc Pd₃Bi nanocrystals were further identified using the XRD technique. As shown in Figure 3a, all the primary peaks in the XRD pattern of the monoclinic Pd₅Bi₂ nanocrystals match well with the Pd₅Bi₂ card (JCPDS no. 33-0212), indicating the formation of the monoclinic phase with high phase-purity and high crystallinity. Importantly, the peaks in the XRD pattern present broadening relative to those in the reference lines on the bottom, revealing that the sample possesses a distribution of nanometer size. For the fcc Pd₃Bi nanocrystals, all the peaks in the XRD pattern are consistent with the previously reported results, ³⁶ further validating the formation of the fcc phase. To determine the chemical valence states of Pd and Bi and composition in as-synthesized nanocrystals, X-ray photoelectron spectroscopic (XPS) experiments were further conducted. As shown in Figure S3, the XPS survey spectrum of the monoclinic Pd₅Bi₂ nanocrystals confirms the coexistence of Pd and Bi, in which the atomic ratio of Pd to Bi was measured to be 72.8:27.2, almost identical to the STEM-EDX and ICP-OES results, implying the uniform composition distribution throughout the nanocrystal. For the Pd 3d spectra shown in Figure 3b, the peaks of metallic Pd located at 335.3 and 340.6 eV with a separation of 5.3 eV in monoclinic Pd₅Bi₂ nanocrystals, exhibit a positive shift compared with the peak positions at 335.1 and 340.4 eV in the case of the fcc Pd₃Bi nanocrystals. Based on the reported peak positions of metallic Pd located at 335.0 and 340.3 eV, the XPS measurement reveals a predominant change in the electronic structure of Pd in monoclinic Pd₅Bi₂ nanocrystals. 11,37 This indicates an increase of the bandwidth of Pd, resulting in a Pd d-band

center downshifting as compared with Pd in fcc Pd₃Bi nanocrystals and monometallic Pd, thus boosting the catalytic activity by weakening the binding affinity between oxygenated species and Pd. Specifically, the ratio of Pd⁰/Pd²⁺ in monoclinic Pd₅Bi₂ nanocrystals was determined as 92.4/7.6 based on the total peak areas of the metallic cations with different valent states, which is higher compared with the value in the fcc Pd₃Bi nanocrystals ($Pd^{0}/Pd^{2+} = 81.7:18.3$). These analyses further corroborate that the surface Pd atoms in $\textit{monoclinic}\ Pd_5Bi_2$ nanocrystals exhibit a much greater antioxidant capability as compared with fcc Pd₃Bi nanocrystals, mainly due to the greatly enhanced electronic interaction between Pd and Bi atoms. For the Bi 4f spectra shown in Figure 3c, the peaks located at 157.3 and 162.6 eV in monoclinic Pd₅Bi₂ nanocrystals can be assigned to the Bi⁰, which are more positive than the peaks located at 157.1 and 162.4 eV in fcc Pd₃Bi nanocrystals, revealing an obvious change of the electronic structure of Bi in monoclinic Pd₅Bi₂ nanocrystals as well. More importantly, no Bi³⁺ peaks were observed in the monoclinic Pd₅Bi₂ nanocrystals while the ratio of Bi⁰/Bi³⁺ was determined to be 67.7/32.3 in the fcc Pd₃Bi nanocrystals. Taken together, these results suggest that the monoclinic Pd5Bi2 nanocrystals exhibited enhanced chemical stability and electronic interaction between Pd and Bi atoms as compared with the fcc Pd₃Bi nanocrystals, thereby benefiting from improving their performance toward ORR in alkaline media.

To further gain insights into the formation mechanism of the *monoclinic* phase in the synthesis, sets of control experiments were conducted to identify the key factors that steer the structure in the final products. It is well-known that the Br ions typically have a strong coordination ability with metallic ions and can selectively adsorb on the specific crystal facets, thus controlling the particle shape of the final products.²⁰ As

expected, when NH₄Br was replaced by NH₄Cl in a typical synthesis, nanocrystals in irregular shapes with a broad size distribution were obtained (Figure S4a), most likely due to the weak interaction of Cl ions with metal seeds as compared to the case with Br ions. The selected area electron diffraction (SAED) characterization confirms the fcc phase (Figure S4b). When the synthesis was carried out in the presence of cetrimonium bromide (CTAB) instead of NH₄Br, wavy nanochains were formed via nanocrystal attachment (Figure S4c). The SAED pattern further suggests an fcc phase from these products (Figure S4d). As such, NH₄Br is very essential to precisely tune the dispersity, morphology, and crystal phase of the final products in this work. Meanwhile, PdCl2 was used as an alternative Pd precursor in a similar synthesis, resulting in nanodendrites with a size of 40 nm (Figure S5), in which the crystal phase was determined as fcc as well by an SAED pattern (Figure S5b). Due to the poor solubility of PdCl₂ in EG, ^{38,39} in this case, not enough Pd2+ ions in solution were provided in the initial stage to develop the morphology and to alter the phase of Pd-Bi nanocrystals. These investigations clearly reveal that both NH₄Br as the capping ligand and K₂PdCl₄ as the Pd precursors play crucial roles in the formation of the monoclinic Pd-Bi nanocrystals.

The catalytic activities of the monoclinic Pd₅Bi₂ nanocrystals, the fcc Pd₃Bi nanocrystals, commercial Pd/C, and commercial Pt/C toward ORR were subsequently evaluated using the rotating-disk electrode (RDE) measurement in 0.1 M KOH. Prior to the electrochemical measurements, the Pd-Bi nanocrystals were loaded on carbon to obtain monoclinic Pd₅Bi₂/C and fcc Pd₃Bi/C catalysts as described in the Supporting Information (SI). All the catalysts were then converted to respective inks using a standard method (SI) for electrochemical evaluation. Figure 4a shows the positive-going ORR polarization curves recorded from the monoclinic Pd₅Bi₂/ C, fcc Pd₃Bi/C, commercial Pd/C, and commercial Pt/C catalysts. It is worth pointing out that the diffusion-limited current density of the commercial Pt/C for the 4e oxygen reduction in 0.1 M O2-saturated KOH can typically reach around -5.7 mA/cm² at a scan rate of 5 mV/s and a rotation rate of 1,600 rpm in terms of the Levich equation. 40 In our case, the ORR polarization curves of the monoclinic Pd₅Bi₂/C catalyst and the fcc Pd₃Bi/C catalyst exhibited a diffusionlimited current density of around -5.8 mA/cm², revealing the 4e⁻ process of forming H₂O, rather than forming the peroxide species via the 2e⁻ pathway. Based on the ORR polarization curves, the monoclinic Pd_5Bi_2/C catalyst showed an $E_{1/2}$ value of 0.93 V vs RHE, which is 6 mV higher than the fcc Pd₃Bi/C, 35 mV higher than Pd/C, and 39 mV higher than Pt/C, revealing the superior alkaline ORR catalytic activity of the monoclinic Pd₅Bi₂/C catalyst relative to the fcc Pd₃Bi/C, Pd/C and Pt/C. To further quantitatively compare the intrinsic activity among all of the catalysts, the MA at 0.9 V, as a benchmark value, was calculated using the Levich equation and then normalized against the Pd or Pt mass-based catalyst on the electrode. At 0.9 V, the MA of the monoclinic Pd₅Bi₂/C (2.05 A/mg_{Pd}) was about 2.2 times as high as that of the fcc Pd₃Bi/C (0.92 A/mg_{Pd}), 6.4 times as high as that of Pd/C (0.32 A/mg_{Pd}) , and 7.3 times as high as that of Pt/C (0.28 A/mg_{Pd}) mg_{Pt}) (Figure 4b). Relative to the fcc Pd₃Bi/C catalyst, the enhancement in MA of the monoclinic Pd₅Bi₂/C catalyst can be mainly attributed to apparent crystal phase discrepancy, approximately excluding the size, composition, and shape effects.

In addition to the great enhancement in MA, the monoclinic Pd₅Bi₂/C catalyst also showed remarkable durability via accelerated durability testing (ADT) with repeatedly potential cycles between 0.60 and 1.00 V at 100 mV/s in O₂-saturated 0.1 M KOH electrolyte, as compared with the fcc Pd₃Bi/C, Pd/ C, and Pt/C. As shown in Figure 4c, the monoclinic Pd₅Bi₂/C catalyst exhibited an activity decay with a $\Delta E_{1/2}$ value of 6 mV after 5,000 cycles and 9 mV after 10,000 cycles, indicating its extraordinary stability. Particularly, the MA at 0.9 V decreased from 2.05 A/mg_{Pd} to 1.98 A/mg_{Pd} after 5,000 cycles, corresponding to a loss of 3% relative to the pristine MA (Figure 4d). After 10,000 cycles, the MA of the monoclinic Pd₅Bi₂/C catalyst was retained at 74% of its original value, while the MA of the fcc Pd₃Bi/C catalyst only retained 46% of its initial value (Figure S6a). In comparison, the MA of the Pd/ C catalyst dropped to 0.17 A/mg_{Pd} after 5,000 cycles of tests, to 0.09 A/mg_{Pd} after 10,000 cycles (Figure S6b). The MA of Pt/C catalyst dropped to 0.12 A/mg_{Pt} after 5,000 cycles of tests, to 0.07 A/mg_{Pt} after 10,000 cycles (Figure S6c). Remarkably, the MA of the monoclinic Pd₅Bi₂/C catalyst after 10,000 cycles was still about 3.6 times as high as that of the fcc Pd₃Bi/C catalyst, 16.9 times as high as that of Pd/C catalyst, and 21.7 times as high as that of Pt/C catalyst. Moreover, in order to probe the origin of the catalytic activity decay after the ADT, the high-angle annular dark-field scanning transmission electron microscopy (HAADF-STEM) (Figure S7a) and HRTEM characterizations (Figure S7b) were performed to identify the size, morphology, and crystal phase changes. Importantly, these structural parameters of the monoclinic Pd₅Bi₂/C catalyst did not show any obvious changes before and after the ADT. Meanwhile, the uniform distribution of Pd and Bi elements throughout the entire nanocrystal after the ADT was further confirmed by the EDX mapping (Figure S7c-e) and corresponding EDX line scan (Figure S7f), in which the ratio of Pd/Bi was measured to be 71.6/28.4, indicating a slightly decreased loss of the total Bi component in comparison with the Pd constituent. Furthermore, the chemical valence states of Pd and Bi after the ADT were also determined by XPS (Figure S8). It shows that the Pd and Bi atoms in the monoclinic Pd₅Bi₂/C catalyst after the ADT still mainly exist in metallic states together with a slight increment in the contents of the Pd and Bi oxidation states. According to the XPS spectra, the ratio of Pd/Bi was calculated to be 71.8/28.2, almost consistent with the EDX results. Combined together, all these results indicate the monoclinic Pd₅Bi₂/C catalyst after the ADT still preserves their pristine size, morphology, composition, and crystal phase, further corroborating their outstanding structural stability and greatly alleviating the leaching of Bi element during the ADT progress.

3. CONCLUSION

In summary, we report a facile and one-pot approach for the synthesis of Pd–Bi nanocrystals with tunable crystal phases, i.e., *monoclinic* Pd₅Bi₂ phase and *fcc* Pd₃Bi phase. To control the crystal structure, it is uncovered that K₂PdCl₄ as the Pd precursors and NH₄Br as the capping ligand play key roles. Impressively, the as-obtained *monoclinic* Pd₅Bi₂/C catalyst exhibits superior electrocatalytic activity and stability toward ORR in alkaline media relative to the *fcc* Pd₃Bi/C counterpart, Pd/C, and Pt/C. This work demonstrates a new strategy for the crystal phase-controlled synthesis of bimetallic nanocrystals and for improving the electrocatalytic performance of ORR. It is highly anticipated that this approach could extend to other

multimetallic nanocrystal systems and even other types of inorganic materials.

ASSOCIATED CONTENT

Supporting Information

The Supporting Information is available free of charge at https://pubs.acs.org/doi/10.1021/jacs.1c08644.

Chemicals, synthesis and characterization, preparation of working electrode and electrochemical measurements, supporting figures of the supplementary experimental results, Figures S1–S8 (PDF)

AUTHOR INFORMATION

Corresponding Authors

Lihua Zhang — Center for Functional Nanomaterials, Brookhaven National Laboratory, Upton, New York 11973, United States; Email: lhzhang@bnl.gov

Jiye Fang — Department of Chemistry, State University of New York at Binghamton, Binghamton, New York 13902, United States; Occid.org/0000-0003-3703-3204; Email: jfang@binghamton.edu

Authors

Ming Zhou − Department of Chemistry, State University of New York at Binghamton, Binghamton, New York 13902, United States; orcid.org/0000-0002-2708-0501

Jiangna Guo – College of Chemistry and Chemical Engineering, Chongqing University, Chongqing 400044, China; orcid.org/0000-0001-5783-5664

Bo Zhao – College of Arts & Sciences Microscopy, Texas Tech University, Lubbock, Texas 79409, United States

Can Li — Department of Chemistry, State University of New York at Binghamton, Binghamton, New York 13902, United States; orcid.org/0000-0001-8894-5110

Complete contact information is available at: https://pubs.acs.org/10.1021/jacs.1c08644

Author Contributions

¹M.Z. and J.G. contributed equally.

Notes

The authors declare no competing financial interest.

ACKNOWLEDGMENTS

M.Z. is primarily supported by the Center for Alkaline-Based Energy Solutions (CABES), an Energy Frontier Research Center program supported by the U.S. Department of Energy, under Grant DE-SC0019445. C.L. acknowledges the National Science Foundation, under Grant DMR 1808383 for its partial support. L.Z. acknowledges the use of TEM facilities for the structural characterizations, at the Center for Functional Nanomaterials, Brookhaven National Laboratory, which is supported by the U.S. DOE, Office of Basic Energy Sciences under Contract No. DE-SC0012704. Partial low-magnification TEM imaging and XPS work is supported by S3IP, State University of New York at Binghamton. We thank Mr. Yang Peng and Mr. Mingjiu Liu for their assistance in the synthesis experiments. We acknowledge Dr. Anju Sharma for her XPS support. We are also grateful to Ms. Elizabeth Jiang for proofreading the manuscript.

REFERENCES

- (1) Liu, M.; Zhao, Z.; Duan, X.; Huang, Y. Nanoscale Structure Design for High-Performance Pt-Based ORR Catalysts. *Adv. Mater.* **2019**, *31*, 1802234.
- (2) Seh, Z. W.; Kibsgaard, J.; Dickens, C. F.; Chorkendorff, I.; Nørskov, J. K.; Jaramillo, T. F. Combining Theory and Experiment in Electrocatalysis: Insights into Materials Design. *Science* **2017**, 355, No. eaad4998.
- (3) Stamenkovic, V. R.; Fowler, B.; Mun, B. S.; Wang, G.; Ross, P. N.; Lucas, C. A.; Marković, N. M. Improved Oxygen Reduction Activity on Pt₃Ni(111) via Increased Surface Site Availability. *Science* **2007**, *315*, 493.
- (4) Zhang, J.; Yang, H.; Fang, J.; Zou, S. Synthesis and Oxygen Reduction Activity of Shape-Controlled Pt₃Ni Nanopolyhedra. *Nano Lett.* **2010**, *10*, 638–644.
- (5) Huang, X.; Zhao, Z.; Cao, L.; Chen, Y.; Zhu, E.; Lin, Z.; Li, M.; Yan, A.; Zettl, A.; Wang, Y. M.; Duan, X.; Mueller, T.; Huang, Y. High-Performance Transition Metal-Doped Pt₃Ni Octahedra for Oxygen Reduction Reaction. *Science* 2015, 348, 1230–1234.
- (6) Wang, D.; Xin, H. L.; Hovden, R.; Wang, H.; Yu, Y.; Muller, D. A.; DiSalvo, F. J.; Abruña, H. D. Structurally Ordered Intermetallic Platinum-Cobalt Core-Shell Nanoparticles with Enhanced Activity and Stability as Oxygen Reduction Electrocatalysts. *Nat. Mater.* **2013**, *12*, 81–87.
- (7) Xiong, Y.; Yang, Y.; DiSalvo, F. J.; Abruña, H. D. Pt-Decorated Composition-Tunable Pd-Fe@Pd/C Core-Shell Nanoparticles with Enhanced Electrocatalytic Activity toward the Oxygen Reduction Reaction. J. Am. Chem. Soc. 2018, 140, 7248–7255.
- (8) Chen, C.; Kang, Y.; Huo, Z.; Zhu, Z.; Huang, W.; Xin, H. L.; Snyder, J. D.; Li, D.; Herron, J. A.; Mavrikakis, M.; Chi, M.; More, K. L.; Li, Y.; Markovic, N. M.; Somorjai, G. A.; Yang, P.; Stamenkovic, V. R. Highly Crystalline Multimetallic Nanoframes with Three-Dimensional Electrocatalytic Surfaces. *Science* **2014**, *343*, 1339.
- (9) Wagner, F. T.; Lakshmanan, B.; Mathias, M. F. Electrochemistry and the Future of the Automobile. *J. Phys. Chem. Lett.* **2010**, *1*, 2204–2219
- (10) Zuo, Y.; Rao, D.; Li, S.; Li, T.; Zhu, G.; Chen, S.; Song, L.; Chai, Y.; Han, H. Atomic Vacancies Control of Pd-Based Catalysts for Enhanced Electrochemical Performance. *Adv. Mater.* **2018**, *30*, 1704171.
- (11) Luo, M.; Zhao, Z.; Zhang, Y.; Sun, Y.; Xing, Y.; Lv, F.; Yang, Y.; Zhang, X.; Hwang, S.; Qin, Y.; Ma, J.-Y.; Lin, F.; Su, D.; Lu, G.; Guo, S. PdMo Bimetallene for Oxygen Reduction Catalysis. *Nature* **2019**, 574, 81–85.
- (12) Jiang, K.; Wang, P.; Guo, S.; Zhang, X.; Shen, X.; Lu, G.; Su, D.; Huang, X. Ordered PdCu-Based Nanoparticles as Bifunctional Oxygen-Reduction and Ethanol-Oxidation Electrocatalysts. *Angew. Chem., Int. Ed.* **2016**, *55*, 9030–9035.
- (13) Guo, J.; Gao, L.; Tan, X.; Yuan, Y.; Kim, J.; Wang, Y.; Wang, H.; Zeng, Y.-J.; Choi, S.-I.; Smith, S. C.; Huang, H. Template-Directed Rapid Synthesis of Pd-Based Ultrathin Porous Intermetallic Nanosheets for Efficient Oxygen Reduction. *Angew. Chem., Int. Ed.* **2021**, *60*, 10942–10949.
- (14) Zamora Zeledón, J. A.; Stevens, M. B.; Gunasooriya, G. T. K. K.; Gallo, A.; Landers, A. T.; Kreider, M. E.; Hahn, C.; Nørskov, J. K.; Jaramillo, T. F. Tuning the Electronic Structure of Ag-Pd Alloys to Enhance Performance for Alkaline Oxygen Reduction. *Nat. Commun.* **2021**, *12*, 620.
- (15) Xu, H.; Shang, H.; Wang, C.; Du, Y. Recent Progress of Ultrathin 2D Pd-Based Nanomaterials for Fuel Cell Electrocatalysis. *Small* **2021**, *17*, 2005092.
- (16) Wang, H.; Luo, W.; Zhu, L.; Zhao, Z.; E, B.; Tu, W.; Ke, X.; Sui, M.; Chen, C.; Chen, Q.; Li, Y.; Huang, Y. Synergistically Enhanced Oxygen Reduction Electrocatalysis by Subsurface Atoms in Ternary PdCuNi Alloy Catalysts. *Adv. Funct. Mater.* **2018**, 28, 1707219.
- (17) Feng, Y.; Shao, Q.; Ji, Y.; Cui, X.; Li, Y.; Zhu, X.; Huang, X. Surface-Modulated Palladium-Nickel Icosahedra as High-Performance

- Non-Platinum Oxygen Reduction Electrocatalysts. Sci. Adv. 2018, 4, No. eaap8817.
- (18) Slanac, D. A.; Hardin, W. G.; Johnston, K. P.; Stevenson, K. J. Atomic Ensemble and Electronic Effects in Ag-Rich AgPd Nanoalloy Catalysts for Oxygen Reduction in Alkaline Media. *J. Am. Chem. Soc.* **2012**, *134*, 9812–9819.
- (19) Lu, X.; Ahmadi, M.; DiSalvo, F. J.; Abruña, H. D. Enhancing the Electrocatalytic Activity of Pd/M (M = Ni, Mn) Nanoparticles for the Oxygen Reduction Reaction in Alkaline Media through Electrochemical Dealloying. *ACS Catal.* **2020**, *10*, 5891–5898.
- (20) Zhou, M.; Li, C.; Fang, J. Noble-Metal Based Random Alloy and Intermetallic Nanocrystals: Syntheses and Applications. *Chem. Rev.* **2021**, *121*, 736–795.
- (21) Xiao, W.; Lei, W.; Gong, M.; Xin, H. L.; Wang, D. Recent Advances of Structurally Ordered Intermetallic Nanoparticles for Electrocatalysis. *ACS Catal.* **2018**, *8*, 3237–3256.
- (22) Sun, D.; Wang, Y.; Livi, K. J. T.; Wang, C.; Luo, R.; Zhang, Z.; Alghamdi, H.; Li, C.; An, F.; Gaskey, B.; Mueller, T.; Hall, A. S. Ordered Intermetallic Pd₃Bi Prepared by an Electrochemically Induced Phase Transformation for Oxygen Reduction Electrocatalysis. *ACS Nano* **2019**, *13*, 10818–10825.
- (23) Wang, Y.; Sun, D.; Chowdhury, T.; Wagner, J. S.; Kempa, T. J.; Hall, A. S. Rapid Room-Temperature Synthesis of a Metastable Ordered Intermetallic Electrocatalyst. *J. Am. Chem. Soc.* **2019**, *141*, 2342–2347.
- (24) Fan, Z.; Zhang, H. Crystal Phase-Controlled Synthesis, Properties and Applications of Noble Metal Nanomaterials. *Chem. Soc. Rev.* **2016**, *45*, 63–82.
- (25) Jiang, G.; Zhu, H.; Zhang, X.; Shen, B.; Wu, L.; Zhang, S.; Lu, G.; Wu, Z.; Sun, S. Core/Shell Face-Centered Tetragonal FePd/Pd Nanoparticles as an Efficient Non-Pt Catalyst for the Oxygen Reduction Reaction. *ACS Nano* **2015**, *9*, 11014–11022.
- (26) Li, J.; Sun, S. Intermetallic Nanoparticles: Synthetic Control and Their Enhanced Electrocatalysis. *Acc. Chem. Res.* **2019**, *52*, 2015–2025.
- (27) Luo, M.; Sun, Y.; Wang, L.; Guo, S. Tuning Multimetallic Ordered Intermetallic Nanocrystals for Efficient Energy Electrocatalysis. *Adv. Energy Mater.* **2017**, *7*, 1602073.
- (28) Chen, Y.; Lai, Z.; Zhang, X.; Fan, Z.; He, Q.; Tan, C.; Zhang, H. Phase Engineering of Nanomaterials. *Nat. Rev. Chem.* **2020**, *4*, 243–256.
- (29) Xiao, F.; Wang, Y.-C.; Wu, Z.-P.; Chen, G.; Yang, F.; Zhu, S.; Siddharth, K.; Kong, Z.; Lu, A.; Li, J.-C.; Zhong, C.-J.; Zhou, Z.-Y.; Shao, M. Recent Advances in Electrocatalysts for Proton Exchange Membrane Fuel Cells and Alkaline Membrane Fuel Cells. *Adv. Mater.* **2021**, 2006292.
- (30) Gilroy, K. D.; Ruditskiy, A.; Peng, H.-C.; Qin, D.; Xia, Y. Bimetallic Nanocrystals: Syntheses, Properties, and Applications. *Chem. Rev.* **2016**, *116*, 10414–10472.
- (31) Xu, D.; Bliznakov, S.; Liu, Z.; Fang, J.; Dimitrov, N. Composition-Dependent Electrocatalytic Activity of Pt-Cu Nanocube Catalysts for Formic Acid Oxidation. *Angew. Chem., Int. Ed.* **2010**, 49, 1282–1285.
- (32) Zhou, M.; Wang, H.; Vara, M.; Hood, Z. D.; Luo, M.; Yang, T.-H.; Bao, S.; Chi, M.; Xiao, P.; Zhang, Y.; Xia, Y. Quantitative Analysis of the Reduction Kinetics Responsible for the One-Pot Synthesis of Pd-Pt Bimetallic Nanocrystals with Different Structures. *J. Am. Chem. Soc.* **2016**, *138*, 12263–12270.
- (33) Maksimuk, S.; Yang, S.; Peng, Z.; Yang, H. Synthesis and Characterization of Ordered Intermetallic PtPb Nanorods. *J. Am. Chem. Soc.* **2007**, *129*, 8684–8685.
- (34) Liu, Z.; Qi, J.; Liu, M.; Zhang, S.; Fan, Q.; Liu, H.; Liu, K.; Zheng, H.; Yin, Y.; Gao, C. Aqueous Synthesis of Ultrathin Platinum/Non-Noble Metal Alloy Nanowires for Enhanced Hydrogen Evolution Activity. *Angew. Chem., Int. Ed.* **2018**, *57*, 11678–11682.
- (35) Yuan, X.; Zhang, Y.; Cao, M.; Zhou, T.; Jiang, X.; Chen, J.; Lyu, F.; Xu, Y.; Luo, J.; Zhang, Q.; Yin, Y. Bi(OH)₃/PdBi Composite Nanochains as Highly Active and Durable Electrocatalysts for Ethanol Oxidation. *Nano Lett.* **2019**, *19*, 4752–4759.

- (36) Xu, H.; Zhang, K.; Yan, B.; Wang, J.; Wang, C.; Li, S.; Gu, Z.; Du, Y.; Yang, P. Ultra-Uniform PdBi Nanodots with High Activity towards Formic Acid Oxidation. *J. Power Sources* **2017**, 356, 27–35.
- (37) Chen, L.; Lu, L.; Zhu, H.; Chen, Y.; Huang, Y.; Li, Y.; Wang, L. Improved Ethanol Electrooxidation Performance by Shortening Pd-Ni Active Site Distance in Pd-Ni-P Nanocatalysts. *Nat. Commun.* **2017**, *8*, 14136.
- (38) Lv, T.; Wang, Y.; Choi, S.-I.; Chi, M.; Tao, J.; Pan, L.; Huang, C. Z.; Zhu, Y.; Xia, Y. Controlled Synthesis of Nanosized Palladium Icosahedra and Their Catalytic Activity towards Formic-Acid Oxidation. *ChemSusChem* **2013**, *6*, 1923–1930.
- (39) Berger, D.; Catrina, G. A.; Vasile, B. S.; Jitaru, I.; Matei, C. Palladium Nanoparticles Synthesis with Controlled Morphology Obtained by Polyol Method. *UPB Sci. Bull. B: Chem. Mater. Sci.* **2010**, 72, 113–120.
- (40) Yang, Y.; Xiong, Y.; Holtz, M. E.; Feng, X.; Zeng, R.; Chen, G.; DiSalvo, F. J.; Muller, D. A.; Abruña, H. D. Octahedral Spinel Electrocatalysts for Alkaline Fuel Cells. *Proc. Natl. Acad. Sci. U. S. A.* **2019**, *116*, 24425.

■ NOTE ADDED AFTER ASAP PUBLICATION

This paper was published ASAP on September 14, 2021 with errors in the TOC/abstract graphic and Figure 4. The graphics were corrected and the revised paper was republished with the issue on September 29, 2021.